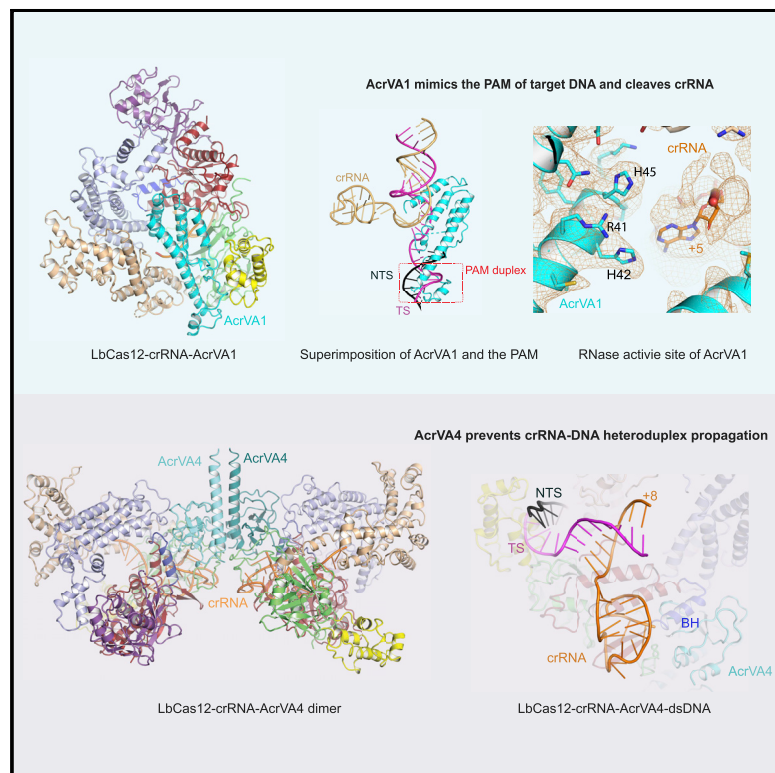


# Cell Host & Microbe

## Structural Basis for the Inhibition of CRISPR-Cas12a by Anti-CRISPR Proteins

### Graphical Abstract



### Authors

Heng Zhang, Zhuang Li,  
Courtney M. Daczkowski,  
Clinton Gabel, Andrew D. Mesecar,  
Leifu Chang

### Correspondence

lchang18@purdue.edu

### In Brief

CRISPR-Cas12a protects bacteria from bacteriophages but is counteracted by inhibitors. Zhang et al. report cryo-EM structures of Cas12a bound to anti-CRISPR proteins. AcrVA1 binds to Cas12a by mimicking the protospacer-adjacent motif (PAM) of a target DNA and cleaves crRNA to inactivate Cas12a. AcrVA4 prevents conformational changes required for Cas12a activation.

### Highlights

- Cryo-EM structure of the Cas12a-crRNA-AcrVA1 complex is presented at 3.5 Å resolution
- AcrVA1 mimics the PAM and cleaves crRNA with an RNase active site in helix α2
- Cryo-EM structure of AcrVA4 dimer bound to Cas12a-crRNA is solved at 3.3 Å resolution
- AcrVA4 stops crRNA-DNA heteroduplex propagation at the +8 position



# Structural Basis for the Inhibition of CRISPR-Cas12a by Anti-CRISPR Proteins

Heng Zhang,<sup>1,4</sup> Zhuang Li,<sup>1,4</sup> Courtney M. Daczkowski,<sup>2</sup> Clinton Gabel,<sup>1</sup> Andrew D. Mesecar,<sup>1,2,3</sup> and Leifu Chang<sup>1,3,5,\*</sup>

<sup>1</sup>Department of Biological Sciences, Purdue University, West Lafayette, IN 47907, USA

<sup>2</sup>Department of Biochemistry, Purdue University, West Lafayette, IN 47907, USA

<sup>3</sup>Purdue University Center for Cancer Research, Purdue University, West Lafayette, IN 47907, USA

<sup>4</sup>These authors contributed equally

<sup>5</sup>Lead Contact

\*Correspondence: lchang18@purdue.edu

<https://doi.org/10.1016/j.chom.2019.05.004>

## SUMMARY

CRISPR-Cas12a (Cpf1), a type V CRISPR-associated nuclease, provides bacterial immunity against bacteriophages and plasmids but also serves as a tool for genome editing. Foreign nucleic acids are integrated into the CRISPR locus, prompting transcription of CRISPR RNAs (crRNAs) that guide Cas12a cleavage of foreign complementary DNA. However, mobile genetic elements counteract Cas12a with inhibitors, notably type V-A anti-CRISPRs (AcrVAs). We present cryoelectron microscopy structures of Cas12a-crRNA bound to AcrVA1 and AcrVA4 at 3.5 and 3.3 Å resolutions, respectively. AcrVA1 is sandwiched between the recognition (REC) and nuclease (NUC) lobes of Cas12a and inserts into the binding pocket for the protospacer-adjacent motif (PAM), a short DNA sequence guiding Cas12a targeting. AcrVA1 cleaves crRNA in a Cas12a-dependent manner, inactivating Cas12a-crRNA complexes. The AcrVA4 dimer is anchored around the crRNA pseudoknot of Cas12a-crRNA, preventing required conformational changes for crRNA-DNA heteroduplex formation. These results uncover molecular mechanisms for CRISPR-Cas12a inhibition, providing insights into bacteria-phage dynamics.

## INTRODUCTION

In bacteria and archaea, clustered regularly interspaced short palindromic repeats (CRISPR) and CRISPR-associated (Cas) proteins provide acquired immunity against bacteriophage and plasmids (Marraffini, 2015; Mohanraju et al., 2016; Sorek et al., 2013; Wright et al., 2016). The CRISPR-Cas defense pathway involves three stages. First, the foreign nucleic acids (protospacers) are integrated into the CRISPR locus (1, adaptation or acquisition stage) as spacers, which are subsequently transcribed and matured into CRISPR RNA (crRNA) by Cas proteins or RNase III (2, expression stage). Lastly, Cas nucleases loaded with crRNA cleave and degrade the invasive nucleic acids complementary to crRNA (3, interference stage) (Barrangou and Mar-

raffini, 2014; Van der Oost et al., 2009). Although the mechanistic diversity of target interference is observed among different CRISPR-Cas systems, crRNA-mediated interference is a common feature in all CRISPR-Cas systems. Based on the composition of the interference module, CRISPR-Cas systems are grouped into two distinct classes comprising six types (I–VI) (Makarova et al., 2015; Shmakov et al., 2015; Shmakov et al., 2017). Multi-protein effector complexes are employed by the class 1 system (types I, III, and IV) to mediate interference. In contrast, the class 2 system (types II, V, and VI), widely adapted for biomedical applications, utilizes a single multidomain Cas effector for cleavage.

The Cas9 endonuclease assigned to type II is the most commonly used CRISPR-Cas system for genome engineering applications (Barrangou and Doudna, 2016; Komor et al., 2017). Recently, Cas12a (also known as Cpf1), a type V CRISPR effector protein, has shown robust genome editing efficiency comparable to that of Cas9 (Hur et al., 2016; Kim et al., 2016; Zetsche et al., 2015). Compared to Cas9 that recognizes a G-rich protospacer-adjacent motif (PAM) sequence and generates blunt ends, Cas12a prefers the T-rich PAM sequence and produces an overhanging cut. Additionally, Cas12a is guided by a ~40 nt crRNA that is roughly half the length of the Cas9 guide RNA (gRNA), potentially allowing improvement of delivery efficiency and operability (Kim et al., 2017). Notably, target recognition can stimulate collateral activities of Cas12a to cleave nonspecific single-stranded DNA (ssDNA) (Chen et al., 2018; Gootenberg et al., 2018; Li et al., 2018; Swarts and Jinek, 2019), similar to the target-activated promiscuous single-stranded RNA (ssRNA) degradation observed in Cas13 (Gootenberg et al., 2018). The collateral cleavage has been developed to facilitate nucleic acid detection in molecular diagnostics (Chen et al., 2018; Gootenberg et al., 2018; Gootenberg et al., 2017). Altogether, the CRISPR-Cas12a system provides a promising tool for genome editing and molecular diagnostics.

The overall structure of Cas12a displays a canonical bilobed architecture encompassing a recognition lobe (REC) and a nuclease lobe (NUC) (Dong et al., 2016; Gao et al., 2016; Nishimasu et al., 2017; Stella et al., 2017, 2018; Swarts and Jinek, 2019; Swarts et al., 2017; Yamano et al., 2016, 2017). Between these two lobes is a central cavity responsible for accommodating target DNA. The NUC lobe is composed of the RuvC, Wedge (WED), PAM-interacting (PI), and Nuc domains. The nuclease activity site is located in the RuvC domain, and a characteristic



bridge helix (BH) motif within the RuvC domain interacts with the REC lobe. The PI domain plays an important role in PAM recognition. The REC lobe contains REC1 and REC2 domains, which recognize the crRNA-DNA heteroduplex.

Mobile genetic elements (MGE) have evolved antidefense mechanisms to evade CRISPR interference (Pawluk et al., 2018). Anti-CRISPR (Acr) proteins are encoded and employed by MGE to inactivate CRISPR-Cas systems, potentially providing programmable “off-switch” tools for CRISPR applications. Most recently, five anti-CRISPR proteins that target CRISPR-Cas12a (AcrVA1–5) have been identified in *Moraxella bovoculi* by two groups (Marino et al., 2018; Watters et al., 2018). Among them, AcrVA1, AcrVA4, and AcrVA5 display inhibitory effects on Cas12a both *in vivo* and *in vitro*. Interestingly, multiple Cas12a orthologs are blocked by these three inhibitors, revealing cross-species inhibitory activity. AcrVA1 broadly inhibits the orthologous CRISPR-Cas12a systems, while AcrVA4 and AcrVA5 fail to block Cas12a from *Acidaminococcus* sp. BV3L6 (Marino et al., 2018; Watters et al., 2018). Cas12a-mediated DNA cleavage involves several steps. First, Cas12a-crRNA ribonucleoprotein binds to the PAM duplex (1, PAM recognition), and initiates dsDNA unwinding (2, dsDNA unwinding). Then, the seed sequence forms base pairs (bp) with the unwound target strand DNA (3, seed complementation), followed by crRNA-DNA heteroduplex formation (4, R-loop formation), a process coupled with conformational rearrangements of Cas12a that allow subsequent DNA cleavage (5, catalysis) (Stella et al., 2017, 2018; Swarts et al., 2017). However, it is not clear which step can be blocked by AcrVA proteins. To reveal the underlying inhibition mechanisms for AcrVA1 and AcrVA4, we determined the cryo-EM structures of Cas12a-crRNA ribonucleoprotein in complex with AcrVA1 and AcrVA4 at resolutions of 3.5 and 3.3 Å, respectively. Structural analysis reveals a mechanistic diversity of CRISPR-Cas12a inhibition that could advance the development of tools for conditional manipulation of CRISPR-Cas12a.

## RESULTS

### AcrVA Proteins Bind to Cas12a in Distinct Fashions

AcrVA proteins have been reported recently to inactivate the CRISPR-Cas12a system (Marino et al., 2018; Watters et al., 2018). Given that Cas9 proteins are blocked by direct physical interactions with inhibitor proteins (Dong et al., 2017; Harrington et al., 2017; Shin et al., 2017; Yang and Patel, 2017), we examined the binding between Cas12a and AcrVA proteins using size exclusion chromatography (SEC) assays. Cas12a from *Lachnospiraceae bacterium ND2006* (LbCas12a) (Zetsche et al., 2015), a commonly employed endonuclease in genome editing, can be cross-inhibited by AcrVA proteins from *Moraxella bovoculi* (Marino et al., 2018; Watters et al., 2018), and thus was used for biochemical and structural characterization. AcrVA1 comigrated with LbCas12a, suggesting formation of the LbCas12a-AcrVA1 complex (Figure S1A). We further tested whether AcrVA1 could bind to the LbCas12a-crRNA ribonucleoprotein. In the presence of AcrVA1, both AcrVA1 and LbCas12a-crRNA eluted in the same fractions (Figure S1B). Given that AcrVA1 alone has a distinct migration profile, our experiments ruled out the possibility that this coelution profile resulted from the overlap of two individual elution profiles. Therefore, AcrVA1 binds to LbCas12a indepen-

dent of crRNA. By contrast, AcrVA4 displayed robust interaction with LbCas12a-crRNA, but not with LbCas12a alone (Figures S1C and S1D), suggesting that AcrVA4 interacts with LbCas12a in a crRNA-dependent manner. These observations suggest that AcrVA1 and AcrVA4 proteins bind to LbCas12a in distinct fashions, possibly representing distinct inhibition mechanisms.

Next, we investigated the inhibitory effects of AcrVA proteins on the endonuclease activity of LbCas12a. Consistent with previous reports (Marino et al., 2018; Watters et al., 2018), in the presence of AcrVA1 or AcrVA4, the cleavage activity of LbCas12a was completely blocked (Figures S1E and S1F). Intriguingly, acrVA4 and acrVA5 coexist in the same gene locus (Watters et al., 2018), prompting us to investigate whether they may interact, and SEC results suggested that they may form a complex (Figures S1G and S1H).

### Cryo-EM Structure of LbCas12a-crRNA-AcrVA1 Complex

To elucidate the molecular basis of Cas12a inhibition by AcrVA1, we used single-particle cryo-EM to determine the structure of the LbCas12a-crRNA-AcrVA1 ternary complex. We first determined a cryo-EM structure of LbCas12a-crRNA alone (Tables S1 and S2). Compared to the crystal structure of LbCas12a-crRNA, an extra density corresponding to the seed sequence (nucleotides 1–5) of crRNA can clearly be seen in our cryo-EM map and the crystal structure of FnCas12a-crRNA (Swarts et al., 2017) (Figure S1I). Additionally, the PI domain involved in crystal packing moves ~6 Å toward the central cavity (Figure S1J), representing a more likely conformation in solution.

Next, we reconstructed a cryo-EM map of the LbCas12a-crRNA-AcrVA1 ternary complex at 3.5 Å resolution (Figures 1 and S2; Tables S1 and S2; Video S1). The density map allowed *de novo* model building for AcrVA1 with main and side chains, with exception of a loop region (residues 60–65), likely due to flexibility. AcrVA1 fits snugly into the central cavity created by the REC and NUC lobes of LbCas12a (Figures 1A–1C). AcrVA1 folds into a fish-hook-shaped architecture composed of five helices and a long loop between helices  $\alpha$ 3 and  $\alpha$ 4 (Figures 1D and 1E). Helices  $\alpha$ 2,  $\alpha$ 3, and  $\alpha$ 5 assemble into a helical bundle, and together with the  $\alpha$ 3- $\alpha$ 4 loop form a hydrophobic core that stabilizes the structure. Structural homology analysis of AcrVA1 revealed no obvious resemblance to any known protein structures (Holm and Laakso, 2016).

Interestingly, further 3D classification of the cryo-EM particle images revealed that an additional density, assigned to a second AcrVA1, can be observed in a small subset of particles (Figure S2F). The second AcrVA1 only appeared in a small portion of particles and was co-occurred with the first one, suggesting that the second binding site is a relatively weak, auxiliary binding site. Therefore, the first binding site is mainly discussed unless otherwise mentioned.

### Interactions between LbCas12a-crRNA and AcrVA1

The AcrVA1-binding cleft of LbCas12a is predominantly positively charged, complementary to the overall negatively charged nature of AcrVA1 (Figures S3A and S3B), indicating a major role of charged and polar interactions in LbCas12a-AcrVA1 association. AcrVA1 can broadly inhibit the orthologous CRISPR-Cas12a systems (Marino et al., 2018; Watters et al., 2018).

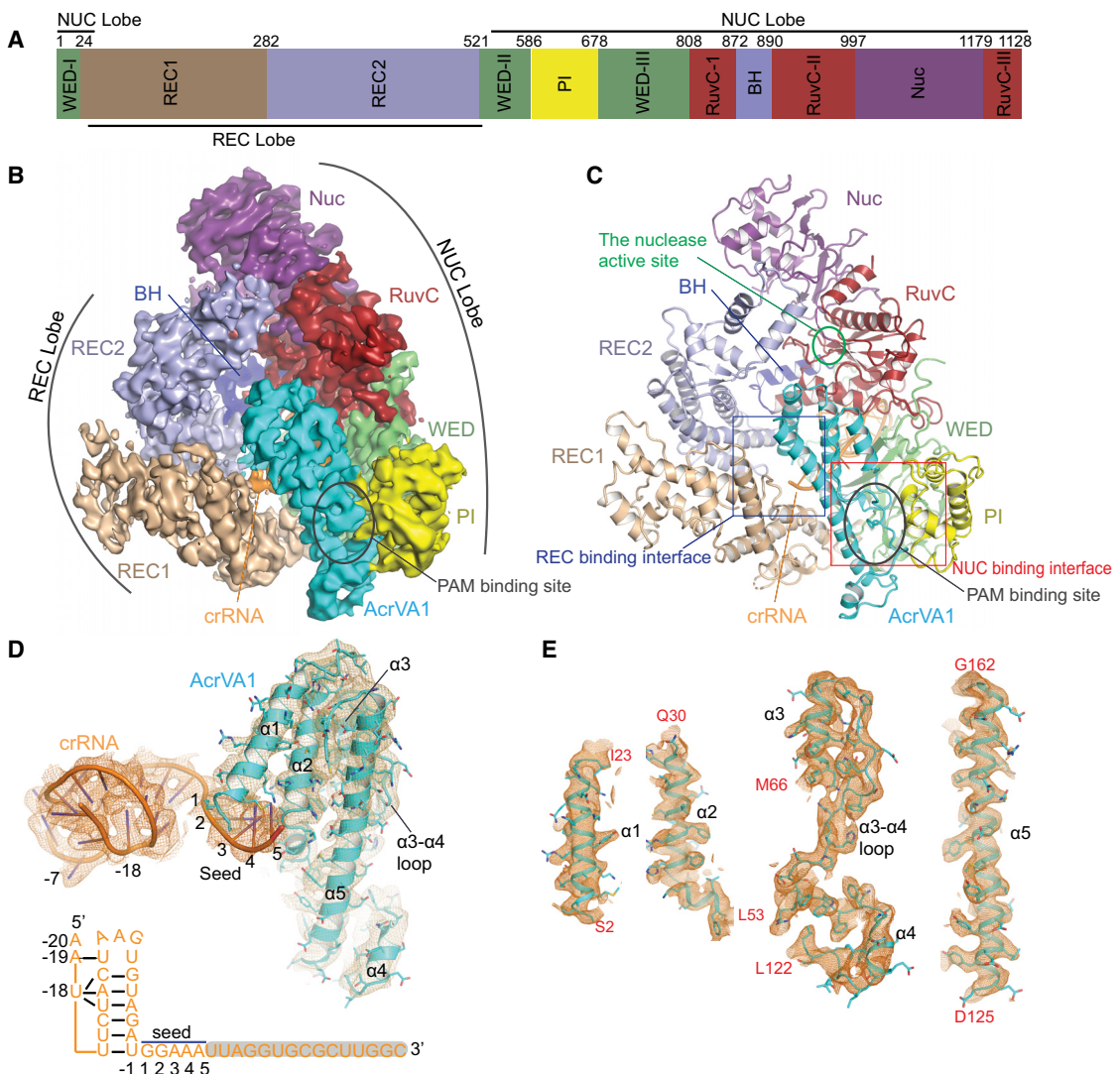


**Figure 1. Structure of LbCas12a-crRNA-AcrVA1 Ternary Complex**

(A) Domain organization of LbCas12a.

(B) Cryo-EM map of LbCas12a-crRNA-AcrVA1 complex color-coded as in (A). AcrVA1 is in cyan.

(C) Cartoon presentation of the overall structure of LbCas12a-crRNA-AcrVA1. The blue and red boxes indicate the interaction interfaces between AcrVA1 and LbCas12a.

(D) Close-up view of crRNA and AcrVA1. Cryo-EM density is shown in mesh. Shown below is a schematic of the crRNA used in this study, with disordered segment shown in a gray background.

(E) Fitting of AcrVA1 to the corresponding cryo-EM densities. See also Figures S1–S3; Tables S1 and S2; Video S1.

Mapping of the evolutionary sequence conservation on the LbCas12a structure revealed that the residues involved in AcrVA1 binding are conserved among Cas12a orthologs (Figure S3C), indicating that AcrVA1 interacts with Cas12a proteins in a similar manner. The overall structure of the AcrVA1-bound ternary complex is similar to that of LbCas12a-crRNA except that the REC1 domain shifts away from the central cavity by  $\sim 10 \text{ \AA}$  to accommodate AcrVA1 (Figure S3D).

The assembly involves two binding interfaces: the NUC- and REC-binding interfaces, with the NUC lobe mainly being responsible for binding AcrVA1. Almost the entire structure of AcrVA1, especially helix  $\alpha 2$  and its succeeding loops ( $\alpha 2$ - $\alpha 3$  loop and

$\alpha 3$ - $\alpha 4$  loop), is involved in the interaction with the NUC lobe. The  $\alpha 2$ - $\alpha 3$  loop binding is mainly stabilized by polar interactions between residues Ser54 and Glu55 from AcrVA1 and residues Trp534, Tyr542, Tyr583, and Gly740 from the WED domain (Figure 2A). The  $\alpha 3$ - $\alpha 4$  loop is bracketed by the WED and PI domains. Specifically, Arg98 of the  $\alpha 3$ - $\alpha 4$  loop presumably forms salt bridges with Asp541 of the WED domain, and the preceding Asp95 establishes hydrogen bonds with Tyr542 of the WED domain (Figure 2A). Additionally, the  $\alpha 3$ - $\alpha 4$  loop is anchored to the PI domain mainly through interaction between Ser96 and Lys595 (Figure 2A). Tyr128 and Tyr132 in helix  $\alpha 5$  engage residues Asp541 and Gln529 of the WED domain, respectively

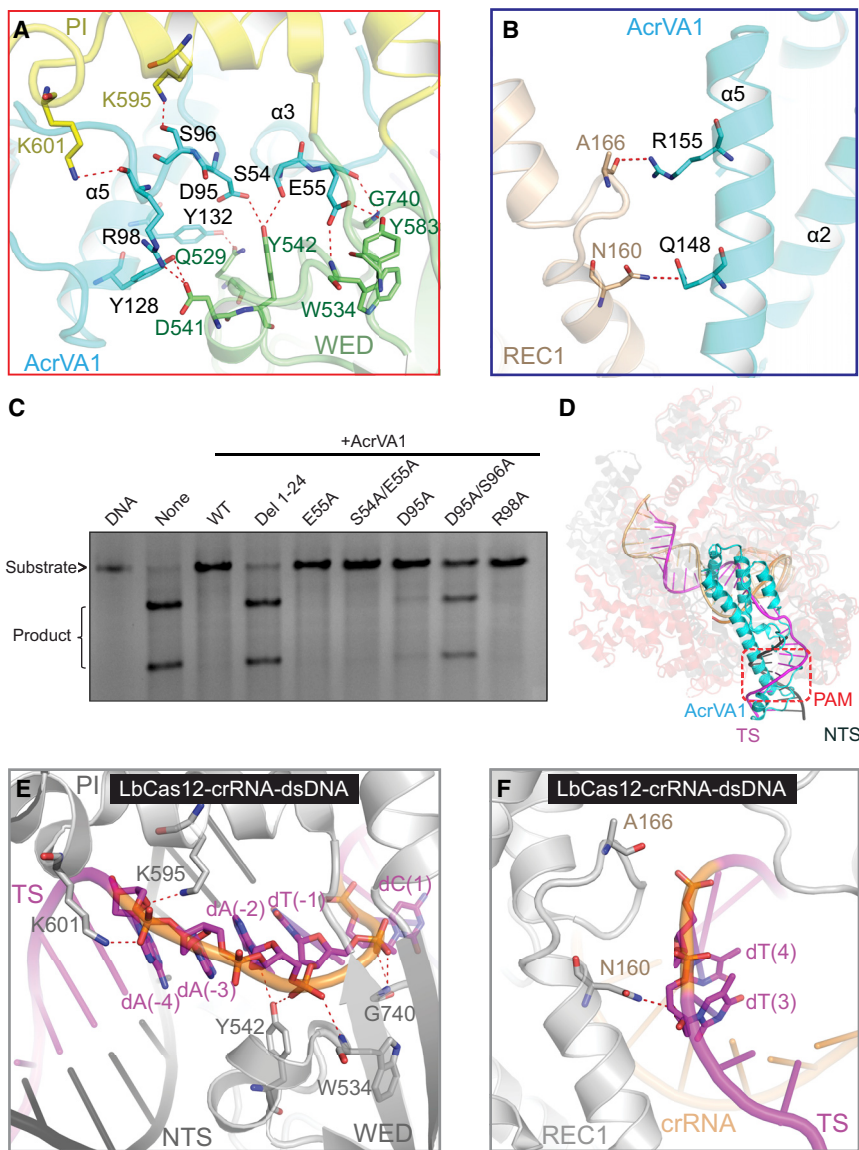


**Figure 2. Interactions between LbCas12a and AcrVA1**

(A) Close-up view of LbCas12a-AcrVA1 interactions involved in the NUC lobe. Observed interactions are shown as red dashed lines.

(B) Close-up view of LbCas12a-AcrVA1 interactions involved in the REC1 domain in the REC lobe.

(C) *In vitro* DNA cleavage assay of LbCas12a in the presence of wild-type, truncated, and mutated AcrVA1.

(D) Superimposition of the structures of AcrVA1-bound LbCas12a-crRNA (this study, LbCas12a shown in transparent red) and the dsDNA-bound LbCas12a-crRNA (PDB: 5XUS, LbCas12a shown in transparent gray). Target (TS) and non-target strands (NTSs) of the PAM duplex are colored in magenta and black, respectively.

(E and F) Interactions between LbCas12a and PAM duplex from a structure of LbCas12a-crRNA-dsDNA complex (PDB: 5XUS). See also Figure S3 and Video S1.

### AcrVA1 Binds to Cas12a by Mimicking PAM

Structural comparisons of AcrVA1-bound LbCas12a-crRNA with DNA-bound LbCas12a-crRNA revealed that AcrVA1 occupies the PAM-duplex-binding groove on LbCas12a (Figure 2D). Residue Gly740 of the WED domain, which is reported to interact with dT(-1) of the PAM sequence, is blocked by Glu55 of AcrVA1 (Yamano et al., 2017) (Figures 2A and 2E). Residues Trp534 and Tyr542 of the WED domain that coordinate dA(-2) of the PAM duplex are bound by the  $\alpha$ 3-2 loop and the  $\alpha$ 3-4 loop (Figures 2A and 2E) (Yamano et al., 2017). Lys601 of the PI domain engaging interaction with dA(-4) base is buttressed by the  $\alpha$ 3-4 loop, establishing a polar

interaction with Arg98 of AcrVA1 (Figures 2A and 2E). Importantly, Lys595 of the WED domain, a crucial residue involved in base-specific recognition of PAM sequence, is buttressed by Ser96 of the  $\alpha$ 3-4 loop. In addition, Asn160 of the REC1 domain that forms polar contacts with dT(3) is replaced by Gln148 of AcrVA1 (Figures 2B and 2F).

### Cas12a-Dependent Cleavage of crRNA by AcrVA1

Surprisingly, crRNA was degraded when Cas12a-crRNA was incubated with AcrVA1, an activity not observed for AcrVA4 (Figure S3E). We further investigated crRNA degradation using 15% TBE-urea gel and found that crRNA can be cleaved into two fragments, indicative of an endonuclease activity in this system (Figure 3A). This activity was dependent on the interaction between AcrVA1 and Cas12a, because neither AcrVA1 nor Cas12a alone can cut crRNA (Figure 3A). Furthermore, mutations of key residues (D95A/S96A) involved in the complex formation impaired crRNA cleavage (Figure 3B). However, crRNA cleavage

(Figure 2A). Altogether, the WED domain, especially the WED II segment, contributes predominantly to AcrVA1 binding.

In contrast to the extensive NUC-binding interface, the REC-binding interface is mainly mediated by helix  $\alpha$ 5 of AcrVA1 and the REC1 domain, forming a relatively small interface, supported by the observation that REC1 is flexible in a 3D classification map (Figure S2F, class 2). Helix  $\alpha$ 5 packs diagonally across the REC1 domain (Figures 1C and 2B). At the C terminus of helix  $\alpha$ 5, polar interactions are made between Gln148 and Arg155 of AcrVA1 and Asn160 and Ala166 of the REC1 domain, respectively (Figure 2B).

To validate the functional importance of the interacting residues in AcrVA1, we introduced alanine substitution into AcrVA1 and carried out cleavage assays. Compared to wild-type (WT) AcrVA1 that completely inhibits Cas12a activity, the double mutant D95A/S96A significantly impaired the AcrVA1-mediated inhibition, demonstrating the importance of the interactions involving Asp95 and Ser96 (Figure 2C).

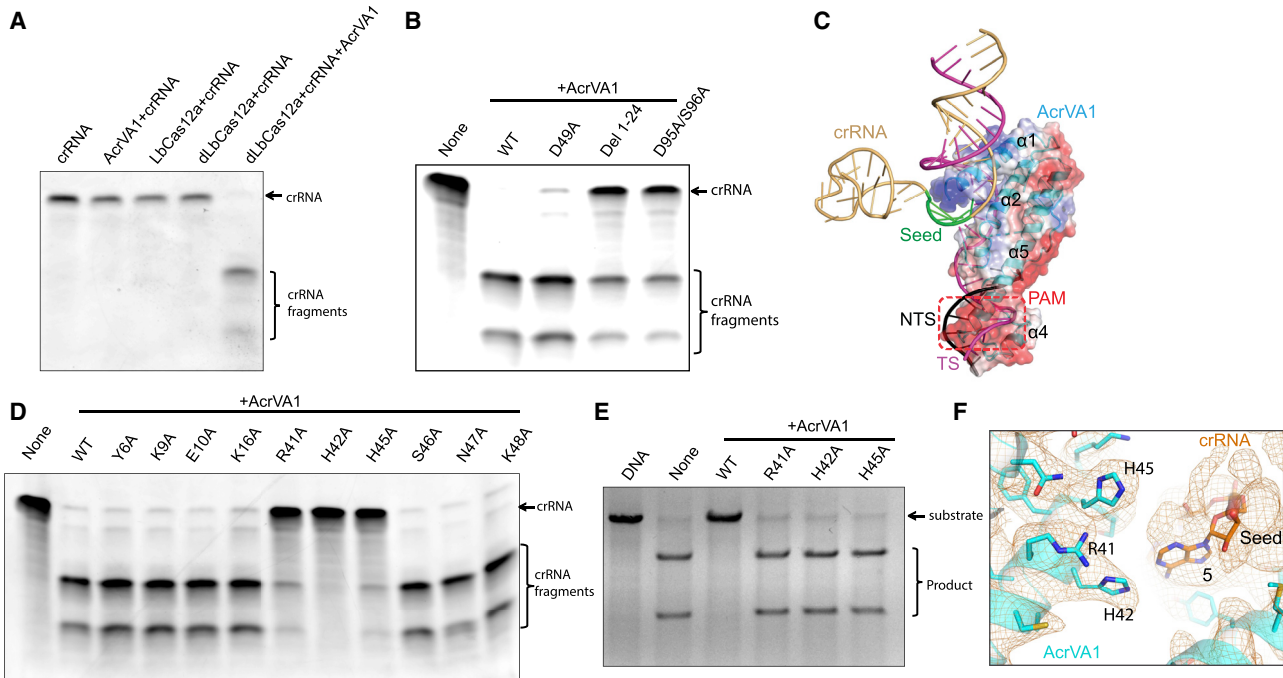


**Figure 3.** AcrVA1 Cleaves crRNA in a Cas12a-Dependent Manner

- (A) A TBE-urea denaturing gel showing crRNA cleavage by the AcrVA1-bound LbCas12a-crRNA complex. dLbCas12a: dead mutant LbCas12a.  
 (B) D95A/S96A mutant reduced the RNase activity of AcrVA1.  
 (C) Electrostatic potential surface of AcrVA1. The positively charged helices  $\alpha$ 1-2 function as a clamp that tethers the seed segment of crRNA (green).  
 (D) Representative denaturing gels showing the crRNA cleavage by either the WT AcrVA1 or the mutants of the helices  $\alpha$ 1-2.  
 (E) AcrVA1 mutants with reduced RNase activity (R41A, H42A, and H45A) failed to inhibit LbCas12a.  
 (F) Key residues for RNase activity (R41, H42, and H45) are located in helix  $\alpha$ 2 and are close to the +5 position of crRNA. See also Figure S3.

was not dependent on a catalytically active Cas12a (Figure 3A), suggesting the presence of a distinct active site. Our structure revealed that the positively charged helices  $\alpha$ 1-2 of AcrVA1 clamp onto crRNA, indicating a likely active site in helices  $\alpha$ 1-2 (Figure 3C). To test this hypothesis, we introduced alanine substitutions for charged or polar residues in helices  $\alpha$ 1-2 around crRNA. Strikingly, R41A or H45A mutations significantly reduced while H42A almost completely abolished crRNA cleavage (Figure 3D). Consistently, the DNA cleavage activity of LbCas12a was restored in the presence of those mutations (Figure 3E), suggesting the importance of AcrVA1-mediated crRNA cleavage in the inhibition of Cas12a activity. Arg41, His42, and His45 are located in helix  $\alpha$ 2, which is close to the position +5 of crRNA (Figure 3F). These results suggest that those three residues constitute the nuclease catalytic site of AcrVA1.

#### Cryo-EM Structure of LbCas12a-crRNA-AcrVA4 Complex

To understand the molecular basis of Cas12a inhibition by AcrVA4, we analyzed the structure of the LbCas12a-crRNA-AcrVA4 complex by cryo-EM (Figures 4 and S4; Tables S1 and S2; Video S2). We also analyzed the complex formed by LbCas12a-crRNA and AcrVA4-AcrVA5 by cryo-EM and obtained essentially the same structure (Figures S5A and S5B), with no EM density corresponding to AcrVA5, indicating that AcrVA5 is likely to be flexible, or AcrVA5 may have disassociated from the LbCas12a-crRNA-AcrVA4 complex.

For the majority of the particles, one LbCas12a-crRNA was bound to an AcrVA4 dimer. We reconstructed a map at 3.3 Å resolution (Figures 4A, 4C, and S4F-S4H). By 3D classification, we found that a subset of particles has two copies of LbCas12a-crRNA bound to an AcrVA4 dimer. We also reconstructed the structure to 3.3 Å resolution with 2-fold symmetry (Figures S4K-S4M). The complex has a butterfly-shaped architecture with a length of ~200 Å (Figures 4B and 4D). In agreement with our cryo-EM observation, two complex species (1:2 and 2:2 stoichiometric ratios) were present in solution, suggesting dynamic equilibrium of these two species (Figure S5C). Structures of LbCas12a-crRNA in both species were nearly identical with a root mean square deviation (RMSD) value of 0.563 Å, indicating that binding of a second LbCas12a-crRNA does not change the existing structure. Two AcrVA4 protomers aligned well with an RMSD value of 0.472 Å.

Dimerization of AcrVA4 in our cryo-EM structures is consistent with the SEC assay (Figure S5D). Binding to LbCas12a occurs in the C-terminal segment of AcrVA4 (residues 120–234), which folds into a globular domain with antiparallel  $\beta$  sheets flanked by two  $\alpha$  helices (Figures 4E–4G). AcrVA4 displays no significant similarity to any known structures (Holm and Laakso, 2016). Protruding from the globular domain is helix  $\alpha$ 1 (residues 120–146) that primarily drives the dimerization of AcrVA4 by electrostatic interactions (Figure S5E). The cryo-EM density corresponding to the N-terminal portion (residues 1–119) of AcrVA4 is poorly

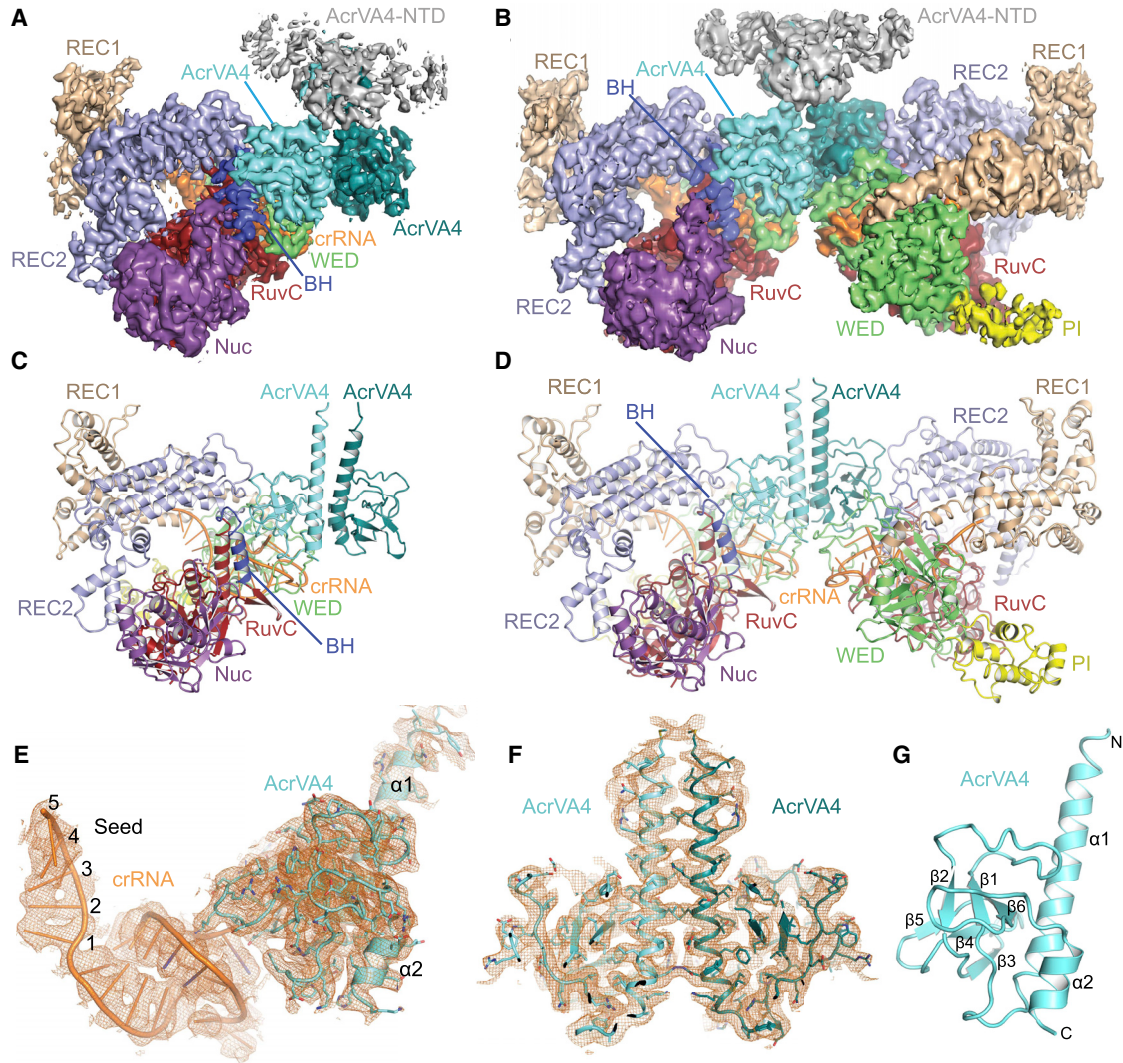


**Figure 4. Structure of LbCas12a-crRNA-AcrVA4 Complex**

(A and B) Cryo-EM maps of AcrVA4 dimer in complex with one copy (A) or two copies (B) of LbCas12a-crRNA. Color codes are as in Figure 1A. Two AcrVA4 molecules are shown in cyan and teal, respectively.

(C and D) Cartoon presentation of LbCas12a-crRNA-AcrVA4 structures corresponding to (A) and (B).

(E) Close-up view of crRNA and AcrVA4. Cryo-EM density is shown in mesh.

(F) Fitting of AcrVA4 dimer to the corresponding cryo-EM densities.

(G) Cartoon presentation of AcrVA4. See also Figures S4 and S5; Tables S1 and S2; Video S2.

ordered, suggesting that the domain is conformationally heterogeneous (Figures 4A, 4B, S5A, and S5B).

#### Interactions between LbCas12a-crRNA and AcrVA4

Distinct from AcrVA1, AcrVA4 is bound to the periphery of Cas12a-crRNA around the crRNA pseudoknot (Figure 4E), implying mechanistic diversity of AcrVA proteins in targeting Cas12a. AcrVA4 makes extensive charged and polar contacts with LbCas12a-crRNA with a buried surface area of  $\sim 1500 \text{ \AA}^2$ . Isothermal titration calorimetry (ITC) studies showed that AcrVA4 exhibits submicromolar affinity toward LbCas12a-crRNA (Figure S5F). Interactions between AcrVA4 and LbCas12a involve the  $\alpha_1$  helix,  $\beta_3$  strand, and  $\beta_3-\beta_4$ ,  $\beta_4-\beta_5$ , and  $\beta_6-\alpha_2$  loops from AcrVA4, and the REC2 and WED domains, and the BH motif

from LbCas12a (Figures 4G and 5A). AcrVA4 lies over the WED III segment and interacts closely with its  $\beta$ -hairpin loop, which is essential for crRNA recognition (Dong et al., 2016; Gao et al., 2016; Swarts et al., 2017; Yamano et al., 2016, 2017). In particular, a set of charged and polar interactions is observed between Lys148, Glu184, and Arg187 or AcrVA4 and Ser763, His759/Lys768, and Val758 of the WED domain, respectively (Figure 5B). In addition to polar interactions, Ala189 on the  $\beta_3-\beta_4$  loop of AcrVA4 makes hydrophobic contacts with Leu756 of WED III, demarcating one side of the interface. On the other side, Glu204 and Arg206 of AcrVA4 contribute to salt bridges with their respective residues (Lys785 and Glu755) on WED III (Figure 5B).

The BH motif, which bridges the NUC and REC lobes, is buttressed by  $\beta_4-\beta_5$  and  $\beta_6-\alpha_2$  loops of AcrVA4. Ser200 and

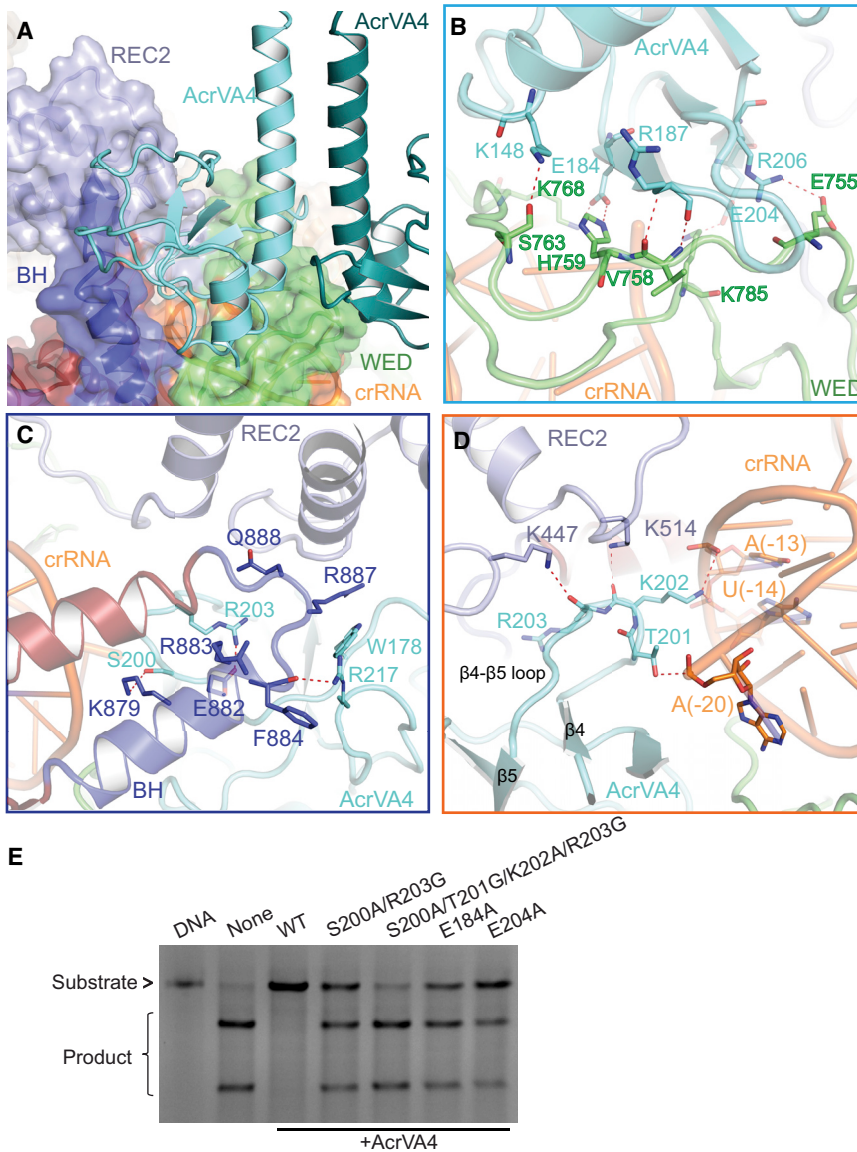


**Figure 5. Interactions between LbCas12a and AcrVA4**

(A) AcrVA4 bound to the pocket created by crRNA, the WED and REC2 domains, and the BH motif.

(B) Detailed interactions between AcrVA4 and WED domain. Interactions are shown as red dashed lines.

(C) Detailed interactions between AcrVA4 and the BH motif.

(D) Detailed interactions between AcrVA4 and LbCas12a-crRNA involving REC2 domain and crRNA.

(E) *In vitro* DNA cleavage assay of LbCas12a in the presence of the wild-type and mutated AcrVA4. See also Video S1.

sociation induces a structural rearrangement of LbCas12a (Dong et al., 2016; Yamano et al., 2017), providing the platform for AcrVA4 binding. Therefore, the crRNA pseudoknot contributes to AcrVA4 binding by direct interactions and inducing conformational changes in Cas12a.

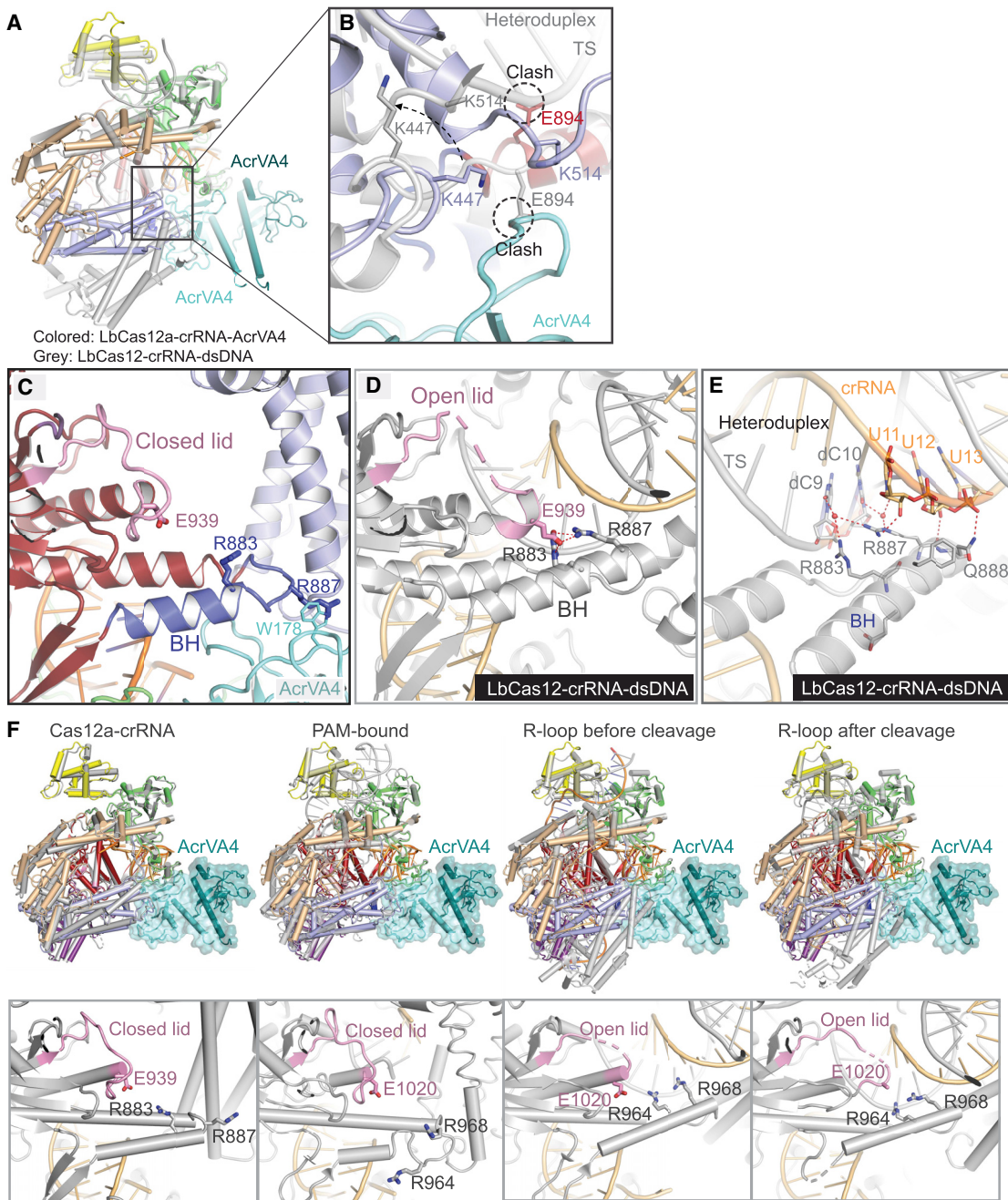
To explore the importance of the observed interactions in our structure, we generated point mutations on AcrVA4 for functional studies. Consistent with our structural observations, the quadruple mutant S200A/T201G/K202A/R203G on the apex of the  $\beta$ 4- $\beta$ 5 loop, which would disrupt the interaction between AcrVA4 and BH/crRNA, impaired the AcrVA4-mediated inhibition, suggesting the importance of the apex of the  $\beta$ 4- $\beta$ 5 loop on the blockage of LbCas12a activity (Figure 5E).

#### AcrVA4 Prevents Conformational Changes Required for Cas12a Activation

In sharp contrast to the intimate interface between AcrVA1 and WED II subdomain, AcrVA4 lies over the WED III segment distal to the PAM-binding pocket, suggesting a distinct blockage mechanism. Structural alignments of AcrVA4-bound LbCas12a with DNA-bound LbCas12a showed that the REC2 domain undergoes considerable conformational changes upon DNA binding (Yamano et al., 2017) (Figure 6A). The REC2 domain shifts toward the crRNA pseudoknot, narrowing the binding pocket for AcrVA4 compared to the AcrVA4-bound structure. Notably, residues Lys447 and Lys514 of the REC2 domain are buried into the intramolecular interaction network in the DNA-bound structure, possibly perturbing their interactions with AcrVA4 (Figure 6B). Additionally, to accommodate the crRNA-DNA heteroduplex, the segment following the BH motif would undergo a conformational change, leading to a rotation of Glu894 and the steric repulsion between Glu894 and AcrVA4 (Figure 6B). As mentioned above, the  $\beta$ 4- $\beta$ 5 loop of AcrVA4—which is surrounded by crRNA, the WED, BH, and REC2 domains—binds tightly to LbCas12a (Figures 5A–5D); thus, AcrVA4 binding would

Arg217 of AcrVA4 form hydrogen bonds with Lys879 and Phe884 of the BH motif, respectively (Figure 5C). A pronounced salt bridge is established between Arg203 of  $\beta$ 4- $\beta$ 5 loop and Glu882 of the BH motif, further fortifying BH-motif binding. Additionally, Trp178 is involved in cation-pi stacking interaction with Arg887 of the BH motif (Figure 5C).

The apex of the  $\beta$ 4- $\beta$ 5 loop of AcrVA4 penetrates deeply into the binding pocket of LbCas12a-crRNA (Figure 5D). In addition to the interaction with the WED III domain and the BH motif mentioned above, the  $\beta$ 4- $\beta$ 5 loop is also involved in binding the REC2 domain and the crRNA pseudoknot. Specifically, Lys202 and Arg203 engage polar contacts with Lys514 and Lys447 of the REC2 domain (Figure 5D). Lys202 is also involved in crRNA binding through salt bridges with phosphate moieties of U(-14) and A(-13). The phosphate backbone of A(-20) in the crRNA 5' handle is bound by Thr201 of the  $\beta$ 4- $\beta$ 5 loop. The observation of crRNA-AcrVA4 association partially explains why AcrVA4 binds to LbCas12a in a crRNA-dependent manner. Moreover, crRNA as-

**Figure 6. Inhibition Mechanism of AcrVA4**

- (A) Superimposition of structures of AcrVA4-bound LbCas12a-crRNA (this study) and dsDNA-bound LbCas12a-crRNA (PDB: 5XUS).
- (B) Structure alignment shows that dsDNA binding induced substantial movements of the residues involved in AcrVA4 binding. Shifts in the residues are indicated by black arrows. The conformation of Glu894 in AcrVA4-bound structure is incompatible with crRNA-DNA heteroduplex in DNA-bound structure, and vice versa.
- (C) AcrVA4 directly interacts with the BH motif and thus would prevent its movement. The lid region is in a closed conformation.
- (D) The BH motif is involved in conformational transition of the lid region upon dsDNA binding. The lid region is in an open conformation.
- (E) The BH motif contributes to stabilization of the crRNA-DNA hybridization upon dsDNA binding. The interaction between the BH motif and the heteroduplex is indicated by red dashed lines.
- (F) Structural comparisons of AcrVA4-bound LbCas12a-crRNA (colored, this study) with LbCas12a-crRNA (gray, PDB: 5ID6), PAM-bound FnCas12a-crRNA (gray, PDB: 6GTC), and R-loop-bound FnCas12a before cleavage (gray, PDB: 5NFV) and after cleavage (gray, PDB: 5MGA). Shown below is a close-up view and the lid region in each state. See also Figure S5.

impede the rotation of Glu894. Structural analysis suggested that the loading of AcrVA4 may occlude the conformational changes required for accommodation and cleavage of DNA, thus locking LbCas12a-crRNA in a nonfunctional state.

Structural comparison between AcrVA4-bound and dsDNA-bound LbCas12a-crRNA complexes showed that the BH motif would shift away from the AcrVA4 binding site and engage the crRNA-DNA heteroduplex upon DNA binding (Figures 6C–6E). Specifically, Arg883 and Gln888 of the BH motif make polar interactions with DNA and crRNA of the heteroduplex, respectively (Figure 6E). Importantly, the side chain of Arg887 would undergo a 180° rotation and establish a hydrogen-bond network with the heteroduplex. However, AcrVA4 directly interacts with the BH motif, especially Arg887, and would prevent the conformational change (Figure 6C), thereby perturbing crRNA-DNA heteroduplex propagation and R-loop formation. Moreover, a lid region (residues 924–940) harboring the catalytic residue Glu925 needs to transit from a “closed” state to an “open” state for cleavage (Stella et al., 2018). R-loop formation would trigger the conformational change of the lid region, wherein Arg883 and Arg887 of the BH motif form salt bridges with Glu939 of the lid region (Figure 6D), facilitating the conformational transition and holding the “open/disordered” state. However, AcrVA4 binding would lock the BH motif and Arg887, thereby hindering the subsequent “open/disordered” state (Figure 6C). As reported recently, the lid region functions as a checkpoint for catalysis at the R-loop formation stage (Stella et al., 2018). Subtle conformational changes may propagate across the whole complex and finally be coupled with the actions of transition and cleavage. Therefore, AcrVA4 binding would prevent the required conformational changes needed for Cas12a activity.

Cas12a undergoes several conformational transitions for the cleavage of dsDNA (Stella et al., 2017, 2018; Swarts et al., 2017) (Figure 6F). AcrVA4 appears not to affect PAM binding and DNA unwinding, as the overall structure of PAM-bound complex is similar to that of the AcrVA4-bound complex (Figure 6F). Furthermore, in both Cas12a-crRNA and PAM-bound complex, the BH motif adopts a conformation that exposes residues required for AcrVA4 binding (Figure 6F), consistent with our electrophoretic mobility shift assay (EMSA), which shows that Cas12a-crRNA-AcrVA4 complex can interact with dsDNA (Figure S5G). However, steric barriers and occupancy of those residues are observed in the presence of fully formed R-loop regardless of pre- or post-cleavage, supporting the model that AcrVA4 would prevent complete R-loop formation.

To verify this model, we prepared Cas12a-crRNA-AcrVA4 in complex with a dsDNA substrate using catalytically inactive Cas12a (D832A) and analyzed the structure by cryo-EM (Figures 7A and S6; Tables S1 and S2). When loaded with DNA, the PAM duplex and an up to 8 bp crRNA-DNA heteroduplex are clearly visible in the map (Figure 7B). Correspondingly, the REC1 domain shifts toward and interacts with the partial crRNA-DNA heteroduplex. As discussed above, propagation of crRNA-DNA heteroduplex requires a rotation of Glu894 and rearrangement of the BH motif (Figures 6B–6E). Our DNA-bound structure showed that indeed those changes are prevented through the interactions between Cas12a and AcrVA4, especially between the

BH motif and AcrVA4, and consequently the crRNA-DNA heteroduplex formation stops at the +8 position (Figure 7B).

## DISCUSSION

The CRISPR-Cas12a system has emerged as a powerful tool for genome editing. AcrVA proteins are found to inhibit the CRISPR-Cas12a system. However, the molecular mechanism by which AcrVA proteins interact with and inhibit Cas12a is not clear. In this study, we determined the atomic structures of Cas12a-crRNA in complex with two recently identified inhibitors (AcrVA1 and AcrVA4) and verified the importance of the AcrVA-Cas12a interactions for inhibition. Our results showed that AcrVA1 occupies the PAM-binding groove and cleaves crRNA, thus inhibiting interference in the Cas12a system, while AcrVA4 binds to the crRNA pseudoknot and prevents the conformational changes required for Cas12a activation.

### The Inhibition Mechanism of AcrVA1

AcrVA1 is predominantly negatively charged, and the binding interface between AcrVA1 and LbCas12a overlaps with the binding interface between the PAM duplex and LbCas12a. Structural analysis suggested that AcrVA1 recognizes Cas12a by mimicking a DNA substrate. Interestingly, AcrlIA2 and AcrlIA4 inactivate CRISPR-Cas9 by mimicking DNA in a manner similar to that of AcrVA1 (Dong et al., 2017; Jiang et al., 2019; Liu et al., 2019; Shin et al., 2017; Yang and Patel, 2017). Thus, a PAM mimic strategy is prevalent in anti-CRISPR proteins.

Strikingly, AcrVA1 is capable of cleaving crRNA in a Cas12a-dependent manner, an observation also reported by a recent study (Knott et al., 2019). Guided by our structure, we performed mutagenesis assays and identified key residues required for the cleavage activity. Arg41, His42, and His45, located in helix  $\alpha$ 2, are critical for crRNA cleavage by AcrVA1. Particularly, alanine substitution of His42 almost completely abolished the AcrVA1-mediated crRNA cleavage (Figure 3D). Helix  $\alpha$ 1 may be involved in the RNase activity of AcrVA1, as deletion of the helix reduced RNase activity (Figure 3B). Our structure, which likely represents a post-cleavage state, showed that the three residues form a pocket close to the seed sequence of crRNA (Figure 3F). The RNase active site of AcrVA1 identified by our work is supported by the recent work mapping the cleavage site of crRNA to the seed sequence (Knott et al., 2019). Our results suggest that AcrVA1 binds to Cas12a by mimicking the PAM of a target DNA and cleaves the crRNA guide, thus inactivating the Cas12a-crRNA complex.

The observation of a second bound AcrVA1 molecule is surprising. The second AcrVA1 occupies the DNA-binding site downstream of crRNA-DNA heteroduplex (Figures S7A–S7C). Structural alignments revealed that the second AcrVA1 would sterically clash with the REC2 domain and crRNA-DNA heteroduplex upon DNA binding (Swarts and Jinek, 2019) (Figures S7C and S7D). The second AcrVA1 seems not to be involved in crRNA cleavage because it does not contact the seed sequence of the crRNA (Figure S7D). It would be interesting to further characterize the function of the second binding site, and our structure provides a blueprint for understanding the mechanism of AcrVA1.

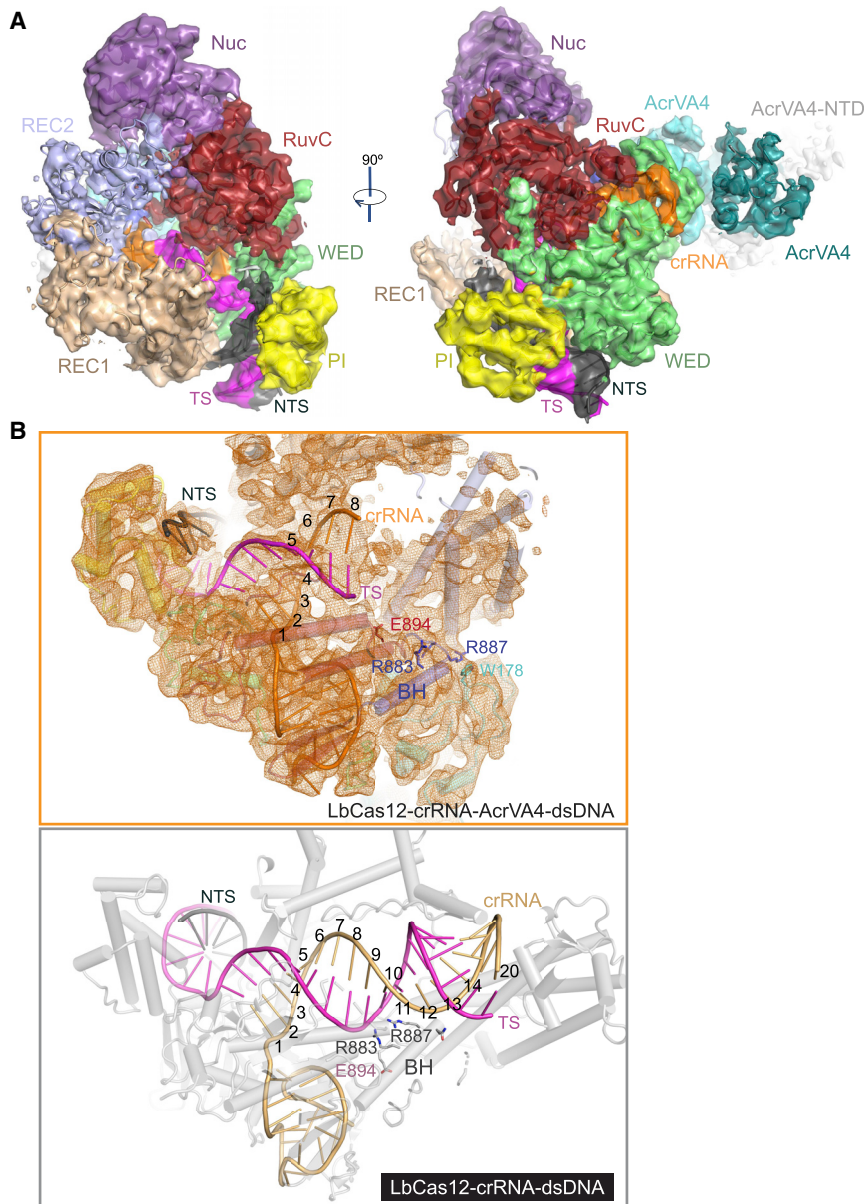


**Figure 7. Structure of Cas12a-crRNA-AcrVA4 in Complex with dsDNA**

(A) Cryo-EM map of LbCas12a-crRNA-AcrVA4-dsDNA complex color-coded as in Figure 1A. Target strand (TS) and non-target strand (NTS) are colored in magenta and black, respectively. (B) Close-up view of the partially formed crRNA-DNA heteroduplex in the context of cryo-EM density map (upper panel) compared to the crystal structure of fully formed crRNA-DNA heteroduplex (bottom panel, PDB: 5XUS). See also Figure S6.

tion of anti-CRISPR proteins. Dimerization seems to be a common feature among some anti-CRISPR proteins (Hynes et al., 2018; Ka et al., 2018; Zhu et al., 2018). It is therefore interesting to further investigate the role of the dimerization event in inhibition among anti-CRISPR proteins.

Like LbCas12a, AsCas12a is also commonly used in genome editing applications. However, AcrVA4 failed to inhibit AsCas12a (Watters et al., 2018). Sequence alignments showed that a helical insertion in the hairpin loop covering the 5' handle crRNA pseudoknot is present in AsCas12a but absent in other close orthologs including LbCas12a, MbCas12a, and FnCas12a (Figure S7E). Structural superimposition of AcrVA4-bound LbCas12a with AsCas12a (Gao et al., 2016; Yamano et al., 2016, 2017) revealed substantial steric clashes between AcrVA4 and the helical insertion of AsCas12a (Figure S7F), thereby explaining why AcrVA4 cannot inhibit AsCas12a. This finding suggests that removal of the helical insertion from AsCas12a may make it susceptible to AcrVA4 inhibition, therefore broadening the application potential of AcrVA4. The absence of the helical insertion in Cas12a

may also be applied to predict the inhibition spectrum of AcrVA4 among Cas12a members.

The genes *acrVA4* and *acrVA5* co-occur in the same gene locus, and AcrVA5 may form a complex with AcrVA4 (Figure S1G); a complex can also be purified by coexpression in *E. coli*. We did not observe any cryo-EM density corresponding to AcrVA5 in our reconstructions. The inhibition of AcrVA4-AcrVA5 was observed similarly to that of AcrVA4 alone, so it is not clear whether the formation of AcrVA4-AcrVA5 is physiologically relevant. A recent study suggests that AcrVA5 functions as an acetyltransferase to modify a lysine residue that is required for PAM recognition, thereby inhibiting Cas12a (Dong et al., 2019). It would be interesting to investigate whether AcrVA4 and AcrVA5 could regulate each other.

In summary, our cryo-EM structures of Cas12a-crRNA in complex with AcrVA1 and AcrVA4 shed light on molecular

### The Inhibition Mechanism of AcrVA4

Our data showed that AcrVA4 inhibits Cas12a by restraining required conformational changes for the complete R-loop formation and activation of Cas12a. The crRNA-DNA heteroduplex formation stops at the +8 position, indicating that this position may be an important checkpoint for Cas12a activation. Activation of Cas12a requires the assembly of at least 16 bp between the target strand and crRNA (Stella et al., 2018), thus AcrVA4 locks Cas12a in an intermediate conformation, preventing the activation of Cas12a.

AcrVA4 behaves as a dimer in solution and induces dimerization of LbCas12a-crRNA. Similarly, AcrIIC3 is also reported to induce dimerization of Cas9 and may hinder R-loop formation (Harrington et al., 2017). Although both the sequence and structure of AcrVA4 are distinct from those of AcrIIC3, a similar inhibition mechanism implies convergent function evolu-

details underlying their distinct inhibitory mechanisms against Cas12a. Anti-CRISPR proteins have been harnessed for control of Cas9-mediated gene editing in human cells (Bubeck et al., 2018; Nakamura et al., 2019). Our findings presented here could serve as a foundation for the development of “off-switch” tools for the CRISPR-Cas12a techniques in the future.

## STAR★METHODS

Detailed methods are provided in the online version of this paper and include the following:

- KEY RESOURCES TABLE
- CONTACT FOR REAGENT AND RESOURCE SHARING
- EXPERIMENTAL MODEL AND SUBJECT DETAILS
- METHOD DETAILS
  - Protein Expression and Purification
  - Mutagenesis
  - Size Exclusion Chromatography
  - *In Vitro* DNA Cleavage Assay
  - crRNA Cleavage Assay
  - Isothermal Titration Calorimetry
  - Electrophoretic Mobility Shift Assay
  - Electron Microscopy
  - Image Processing
  - Model Building and Refinement
  - Visualization
- DATA AND SOFTWARE AVAILABILITY

## SUPPLEMENTAL INFORMATION

Supplemental Information can be found online at <https://doi.org/10.1016/j.chom.2019.05.004>.

## ACKNOWLEDGMENTS

We thank Thomas Klose, Valorie Bowman, and Wen Jiang for help with cryo-EM data collection, Steven Wilson for support in computation, Hengyao Niu for help in ITC and EMSA assays, and John Tesmer and David Barford for helpful discussion. Cryo-EM data were acquired at the Purdue Cryo-EM Facility. L.C. is supported by the Department of Biological Sciences at Purdue University in the United States.

## AUTHOR CONTRIBUTIONS

H.Z. and L.C. designed the research. H.Z. prepared samples and performed biochemical assays with help from Z.L. and C.G. C.M.D. and A.D.M. performed ITC experiments. Z.L., H.Z., and L.C. collected and processed cryo-EM data. All authors analyzed the data. H.Z., Z.L., and L.C. wrote the paper with input from all authors.

## DECLARATION OF INTERESTS

The authors declare no competing interests.

Received: February 22, 2019

Revised: April 15, 2019

Accepted: May 9, 2019

Published: May 30, 2019

## REFERENCES

- Afonine, P.V., Poon, B.K., Read, R.J., Sobolev, O.V., Terwilliger, T.C., Urzhumtsev, A., and Adams, P.D. (2018). Real-space refinement in PHENIX for cryo-EM and crystallography. *Acta Crystallogr. D Struct. Biol.* 74, 531–544.
- Ashkenazy, H., Erez, E., Martz, E., Pupko, T., and Ben-Tal, N. (2010). ConSurf 2010: calculating evolutionary conservation in sequence and structure of proteins and nucleic acids. *Nucleic Acids Res.* 38, W529–W533.
- Barrangou, R., and Doudna, J.A. (2016). Applications of CRISPR technologies in research and beyond. *Nat. Biotechnol.* 34, 933–941.
- Barrangou, R., and Marraffini, L.A. (2014). CRISPR-CAS systems: prokaryotes upgrade to adaptive immunity. *Mol. Cell* 54, 234–244.
- Bubeck, F., Hoffmann, M.D., Harteveld, Z., Aschenbrenner, S., Bietz, A., Waldhauer, M.C., Börner, K., Fakhri, J., Schmelas, C., Dietz, L., et al. (2018). Engineered anti-CRISPR proteins for optogenetic control of CRISPR-Cas9. *Nat. Methods* 15, 924–927.
- Chen, J.S., Ma, E., Harrington, L.B., Da Costa, M., Tian, X., Palefsky, J.M., and Doudna, J.A. (2018). CRISPR-Cas12a target binding unleashes indiscriminate single-stranded DNase activity. *Science* 360, 436–439.
- Dong, D., Guo, M., Wang, S., Zhu, Y., Wang, S., Xiong, Z., Yang, J., Xu, Z., and Huang, Z. (2017). Structural basis of CRISPR-SpyCas9 inhibition by an anti-CRISPR protein. *Nature* 546, 436–439.
- Dong, D., Ren, K., Qiu, X., Zheng, J., Guo, M., Guan, X., Liu, H., Li, N., Zhang, B., Yang, D., et al. (2016). The crystal structure of Cpf1 in complex with CRISPR RNA. *Nature* 532, 522–526.
- Dong, L., Guan, X., Li, N., Zhang, F., Zhu, Y., Ren, K., Yu, L., Zhou, F., Han, Z., Gao, N., et al. (2019). An anti-CRISPR protein disables type V Cas12a by acetylation. *Nat. Struct. Mol. Biol.* 26, 308–314.
- Emsley, P., Lohkamp, B., Scott, W.G., and Cowtan, K. (2010). Features and development of coot. *Acta Crystallogr. D Biol. Crystallogr.* 66, 486–501.
- Gao, P., Yang, H., Rajashankar, K.R., Huang, Z., and Patel, D.J. (2016). Type V CRISPR-CAS Cpf1 endonuclease employs a unique mechanism for crRNA-mediated target DNA recognition. *Cell Res.* 26, 901–913.
- Gootenberg, J.S., Abudayyeh, O.O., Kellner, M.J., Joung, J., Collins, J.J., and Zhang, F. (2018). Multiplexed and portable nucleic acid detection platform with Cas13, Cas12a, and Csm6. *Science* 360, 439–444.
- Gootenberg, J.S., Abudayyeh, O.O., Lee, J.W., Essletzbichler, P., Dy, A.J., Joung, J., Verdine, V., Donghia, N., Daringer, N.M., and Freije, C.A. (2017). Nucleic Acid Detection with CRISPR-Cas13a/C2c2. *Science* 356, 438–442.
- Grant, T., Rohou, A., and Grigorieff, N. (2018). cisTEM, user-friendly software for single-particle image processing. *Elife* 7, e35383.
- Harrington, L.B., Doxzen, K.W., Ma, E., Liu, J.J., Knott, G.J., Edraki, A., Garcia, B., Amrani, N., Chen, J.S., Cofsky, J.C., et al. (2017). A broad-spectrum inhibitor of CRISPR-Cas9. *Cell* 170, 1224–1233.
- Holm, L., and Laakso, L.M. (2016). Dali server update. *Nucleic Acids Res.* 44, W351–W355.
- Hur, J.K., Kim, K., Been, K.W., Baek, G., Ye, S., Hur, J.W., Ryu, S.-M., Lee, Y.S., and Kim, J.-S. (2016). Targeted mutagenesis in mice by electroporation of Cpf1 ribonucleoproteins. *Nat. Biotechnol.* 34, 807–808.
- Hynes, A.P., Rousseau, G.M., Agudelo, D., Goulet, A., Amigues, B., Loehr, J., Romero, D.A., Fremaux, C., Horvath, P., Doyon, Y., et al. (2018). Widespread anti-CRISPR proteins in virulent bacteriophages inhibit a range of Cas9 proteins. *Nat. Commun.* 9, 2919.
- Jiang, F., Liu, J.J., Osuna, B.A., Xu, M., Berry, J.D., Rauch, B.J., Nogales, E., Bondy-Denomy, J., and Doudna, J.A. (2019). Temperature-responsive competitive inhibition of CRISPR-Cas9. *Mol. Cell* 73, 601–610.
- Ka, D., An, S.Y., Suh, J.Y., and Bae, E. (2018). Crystal structure of an anti-CRISPR protein, AcrlA1. *Nucleic Acids Res.* 46, 485–492.
- Kim, H., Kim, S.T., Ryu, J., Kang, B.C., Kim, J.S., and Kim, S.G. (2017). CRISPR/Cpf1-mediated DNA-free plant genome editing. *Nat. Commun.* 8, 14406.

- Kim, Y., Cheong, S.A., Lee, J.G., Lee, S.W., Lee, M.S., Baek, I.J., and Sung, Y.H. (2016). Generation of knockout mice by Cpf1-mediated gene targeting. *Nat. Biotechnol.* 34, 808–810.
- Knott, G.J., Thornton, B.W., Lobba, M.J., Liu, J.J., Al-Shayeb, B., Watters, K.E., and Doudna, J.A. (2019). Broad-spectrum enzymatic inhibition of CRISPR-Cas12a. *Nat. Struct. Mol. Biol.* 26, 315–321.
- Komor, A.C., Badran, A.H., and Liu, D.R. (2017). CRISPR-based technologies for the manipulation of eukaryotic genomes. *Cell* 168, 20–36.
- Lander, G.C., Stagg, S.M., Voss, N.R., Cheng, A., Fellmann, D., Pulokas, J., Yoshioka, C., Irving, C., Mulder, A., Lau, P.W., et al. (2009). Appion: an integrated, database-driven pipeline to facilitate EM image processing. *J. Struct. Biol.* 166, 95–102.
- Li, S.Y., Cheng, Q.X., Liu, J.K., Nie, X.Q., Zhao, G.P., and Wang, J. (2018). CRISPR-Cas12a has both cis- and trans-cleavage activities on single-stranded DNA. *Cell Res.* 28, 491–493.
- Liu, L., Yin, M., Wang, M., and Wang, Y. (2019). Phage AcrlA2 DNA mimicry: structural basis of the CRISPR and anti-CRISPR arms race. *Mol. Cell* 73, 611–620.
- Makarova, K.S., Wolf, Y.I., Alkhnbashi, O.S., Costa, F., Shah, S.A., Saunders, S.J., Barrangou, R., Brouns, S.J., Charpentier, E., Haft, D.H., et al. (2015). An updated evolutionary classification of CRISPR-CAS systems. *Nat. Rev. Microbiol.* 13, 722–736.
- Marino, N.D., Zhang, J.Y., Borges, A.L., Sousa, A.A., Leon, L.M., Rauch, B.J., Walton, R.T., Berry, J.D., Joung, J.K., Kleinstiver, B.P., et al. (2018). Discovery of widespread type I and type V CRISPR-CAS inhibitors. *Science* 362, 240–242.
- Marraffini, L.A. (2015). CRISPR-CAS immunity in prokaryotes. *Nature* 526, 55–61.
- Mohanraju, P., Makarova, K.S., Zetsche, B., Zhang, F., Koonin, E.V., and Van der Oost, J. (2016). Diverse evolutionary roots and mechanistic variations of the CRISPR-CAS systems. *Science* 353, aad5147.
- Nakamura, M., Srinivasan, P., Chavez, M., Carter, M.A., Dominguez, A.A., La Russa, M., Lau, M.B., Abbott, T.R., Xu, X., Zhao, D., et al. (2019). Anti-CRISPR-mediated control of gene editing and synthetic circuits in eukaryotic cells. *Nat. Commun.* 10, 194.
- Nishimasu, H., Yamano, T., Gao, L., Zhang, F., Ishitani, R., and Nureki, O. (2017). Structural basis for the altered PAM recognition by engineered CRISPR-Cpf1. *Mol. Cell* 67, 139–147.e2.
- Pawluk, A., Davidson, A.R., and Maxwell, K.L. (2018). Anti-CRISPR: discovery, mechanism and function. *Nat. Rev. Microbiol.* 16, 12–17.
- Pettersen, E.F., Goddard, T.D., Huang, C.C., Couch, G.S., Greenblatt, D.M., Meng, E.C., and Ferrin, T.E. (2004). UCSF Chimera—a visualization system for exploratory research and analysis. *J. Comp. Chem.* 25, 1605–1612.
- Shin, J., Jiang, F., Liu, J.J., Bray, N.L., Rauch, B.J., Baik, S.H., Nogales, E., Bondy-Denomy, J., Corn, J.E., and Doudna, J.A. (2017). Disabling Cas9 by an anti-CRISPR DNA mimic. *Sci. Adv.* 3, e1701620.
- Shmakov, S., Abudayyeh, O.O., Makarova, K.S., Wolf, Y.I., Gootenberg, J.S., Semenova, E., Minakhin, L., Joung, J., Konermann, S., Severinov, K., et al. (2015). Discovery and functional characterization of diverse class 2 CRISPR-CAS systems. *Mol. Cell* 60, 385–397.
- Shmakov, S., Smargon, A., Scott, D., Cox, D., Pyzocha, N., Yan, W., Abudayyeh, O.O., Gootenberg, J.S., Makarova, K.S., Wolf, Y.I., et al. (2017). Diversity and evolution of class 2 CRISPR-CAS systems. *Nat. Rev. Microbiol.* 15, 169–182.
- Sorek, R., Lawrence, C.M., and Wiedenheft, B. (2013). CRISPR-mediated adaptive immune systems in bacteria and archaea. *Annu. Rev. Biochem.* 82, 237–266.
- Stella, S., Alcón, P., and Montoya, G. (2017). Structure of the Cpf1 endonuclease R-loop complex after target DNA cleavage. *Nature* 546, 559–563.
- Stella, S., Mesa, P., Thomsen, J., Paul, B., Alcón, P., Jensen, S.B., Saligram, B., Moses, M.E., Hatzakis, N.S., and Montoya, G. (2018). Conformational activation promotes CRISPR-Cas12a catalysis and resetting of the endonuclease activity. *Cell* 175, 1856–1871.
- Suloway, C., Pulokas, J., Fellmann, D., Cheng, A., Guerra, F., Quispe, J., Stagg, S., Potter, C.S., and Carragher, B. (2005). Automated molecular microscopy: the new Leginon system. *J. Struct. Biol.* 151, 41–60.
- Swarts, D.C., and Jinek, M. (2019). Mechanistic Insights into the cis- and trans-acting DNase activities of Cas12a. *Mol. Cell* 73, 589–600.
- Swarts, D.C., van der Oost, J., and Jinek, M. (2017). Structural basis for guide RNA processing and seed-dependent DNA targeting by CRISPR-Cas12a. *Mol. Cell* 66, 221–233.
- Van der Oost, J., Jore, M.M., Westra, E.R., Lundgren, M., and Brouns, S.J.J. (2009). CRISPR-based adaptive and heritable immunity in prokaryotes. *Trends Biochem. Sci.* 34, 401–407.
- Watters, K.E., Fellmann, C., Bai, H.B., Ren, S.M., and Doudna, J.A. (2018). Systematic discovery of natural CRISPR-Cas12a inhibitors. *Science* 362, 236–239.
- Wright, A.V., Nuñez, J.K., and Doudna, J.A. (2016). Biology and applications of CRISPR systems: harnessing nature's toolbox for genome engineering. *Cell* 164, 29–44.
- Yamano, T., Nishimasu, H., Zetsche, B., Hirano, H., Slaymaker, I.M., Li, Y., Fedorova, I., Nakane, T., Makarova, K.S., Koonin, E.V., et al. (2016). Crystal structure of Cpf1 in complex with guide RNA and target DNA. *Cell* 165, 949–962.
- Yamano, T., Zetsche, B., Ishitani, R., Zhang, F., Nishimasu, H., and Nureki, O. (2017). Structural basis for the canonical and non-canonical PAM recognition by CRISPR-Cpf1. *Mol. Cell* 67, 633–645.
- Yang, H., and Patel, D.J. (2017). Inhibition mechanism of an anti-CRISPR suppressor AcrlA4 targeting SpyCas9. *Mol. Cell* 67, 117–127.
- Zetsche, B., Gootenberg, J.S., Abudayyeh, O.O., Slaymaker, I.M., Makarova, K.S., Essletzbichler, P., Volz, S.E., Joung, J., Van Der Oost, J., Regev, A., et al. (2015). Cpf1 is a single RNA-guided endonuclease of a class 2 CRISPR-CAS system. *Cell* 163, 759–771.
- Zhang, K. (2016). Gctf: real-time CTF determination and correction. *J. Struct. Biol.* 193, 1–12.
- Zheng, S.Q., Palovcak, E., Armache, J.-P., Verba, K.A., Cheng, Y., and Agard, D.A. (2017). MotionCor2: anisotropic correction of beam-induced motion for improved cryo-electron microscopy. *Nat. Methods* 14, 331–332.
- Zhu, Y., Zhang, F., and Huang, Z. (2018). Structural insights into the inactivation of CRISPR-CAS systems by diverse anti-CRISPR proteins. *BMC Biol.* 16, 32.
- Zivanov, J., Nakane, T., Forsberg, B.O., Kimanis, D., Hagen, W.J., Lindahl, E., and Scheres, S.H. (2018). New tools for automated high-resolution cryo-EM structure determination in RELION-3. *Elife* 7, e42166.

**STAR★METHODS****KEY RESOURCES TABLE**

REAGENT or RESOURCE	SOURCE	IDENTIFIER
Bacterial and Virus Strains		
BL21-CodonPlus (DE3)-RIL	Agilent Technologies	Cat# 230245
Chemicals, Peptides, and Recombinant Proteins		
Terrific Broth (TB)	Thermo fisher scientific	Cat# BP97285
isopropyl β-D-thiogalactopyranoside (IPTG)	Thermo fisher scientific	Cat# R0393
Tris-Base	Thermo fisher scientific	Cat# BP152-1
HEPES	Thermo fisher scientific	Cat# BP310-1
Sodium chloride	Thermo fisher scientific	Cat# S271-10
Glycerol	Thermo fisher scientific	Cat# G33-500
2-Mercaptoethanol	Thermo fisher scientific	Cat# O3446I-100
Magnesium chloride	Thermo fisher scientific	Cat# M33-500
PMSF	Sigma-Aldrich	Cat# P7626
Imidazole	Sigma-Aldrich	Cat# I202-2KG
DTT	Thermo fisher scientific	Cat# AAJ1539722
EDTA	Thermo fisher scientific	Cat# AM9261
Potassium Chloride	Thermo fisher scientific	Cat# P217-500
Agarose	Thermo fisher scientific	Cat# BP1356-500
Ethidium Bromide	Thermo fisher scientific	Cat# BP1302-10
SYBR gold	Thermo fisher scientific	Cat# S11494
Tobacco Etch Virus (TEV) protease	Homemade	N/A
Fspl	New England Biolabs	Cat# R0135L
Proteinase K	New England Biolabs	Cat# P8107S
Critical Commercial Assays		
QIAquick PCR Purification Kit	QIAGEN	Cat# 28106
Ni-NTA agarose resin	QIAGEN	Cat# 30430
HiTrap Q HP	GE Healthcare	Cat# 17115401
HiTrap SP HP	GE Healthcare	Cat# 17115201
Superdex 200 10/300 column	GE Healthcare	Cat# 28990944
Deposited Data		
Cas12a-crRNA coordinate	This study	PDB: 6NME
Cas12a-crRNA map	This study	EMDB: EMD-0449
Cas12a-crRNA-AcrVA1 coordinate	This study	PDB: 6NMD
Cas12a-crRNA-AcrVA1 map	This study	EMDB: EMD-0447
Cas12a-crRNA-(AcrVA1) <sub>2</sub> coordinate	This study	PDB: 6NMC
Cas12a-crRNA-(AcrVA1) <sub>2</sub> map	This study	EMDB: EMD-0446
Cas12a-crRNA-(AcrVA4) <sub>2</sub> coordinate	This study	PDB: 6NMA
Cas12a-crRNA-(AcrVA4) <sub>2</sub> map	This study	EMDB: EMD-0445
(Cas12a-crRNA-AcrVA4) <sub>2</sub> coordinate	This study	PDB: 6NM9
(Cas12a-crRNA-AcrVA4) <sub>2</sub> map	This study	EMDB: EMD-9398
Cas12a-crRNA-(AcrVA4) <sub>2</sub> -DNA coordinate	This study	PDB: 6OMV
Cas12a-crRNA-(AcrVA4) <sub>2</sub> -DNA map	This study	EMDB: EMD-20132
(Cas12a-crRNA-AcrVA4-DNA) <sub>2</sub> map	This study	EMDB: EMD-20182

(Continued on next page)

**Continued**

REAGENT or RESOURCE	SOURCE	IDENTIFIER
Oligonucleotides		
crRNA for the cryo-EM complex and SEC assays: AAUUUCUAC UAAGUGUAGAUGGAAAUUAGGUGCGCUUGGC	IDT	N/A
crRNA for the EMSA, DNA and RNA cleavage assays: AAUUU CUACUAAGUGUAGAUGGAAAUUAGGUGCGCUUGGCAACC	IDT	N/A
Target DNA for the cryo-EM complex: TCTCAAGGTTGCCAAG CGCACCTAATTCCTAAAGGACG	IDT	N/A
Non-target DNA for the cryo-EM complex: CGTCCTTAGGAAA TTAGGTGCGCTTGCAACCTTGAGA	IDT	N/A
Recombinant DNA		
pMBP-LbCas12a	(Chen et al., 2018)	Addgene plasmid # 113431
pET28-MKH8SUMO-AcrVA1	This paper	N/A
pET28-MKH8SUMO-AcrVA1, various mutants	This paper	N/A
pKEW212-MBP-TEV-AcrVA4	(Watters et al., 2018)	Addgene plasmid # 115658
pKEW212-MBP-TEV-AcrVA4, various mutants	This paper	N/A
pET28-MKH8SUMO-AcrVA5	This paper	N/A
pET28-MHL-target DNA	This paper	N/A
Software and Algorithms		
PyMOL	Schrodinger LLC	RRID: SCR_000305
UCSF Chimera	(Pettersen et al., 2004)	RRID: SCR_004097
Phenix	(Afonine et al., 2018)	RRID: SCR_014224
Coot	(Emsley et al., 2010)	RRID: SCR_014222
Relion	(Zivanov et al., 2018)	RRID: SCR_016274
cisTEM	(Grant et al., 2018)	RRID:SCR_016502
Leginon	(Suloway et al., 2005)	RRID: SCR_016731
GCTF	(Zhang, 2016)	RRID: SCR_016500
MotionCor2	(Zheng et al., 2017)	RRID: SCR_016499
Other		
TBE-Urea Gels, 15%	Thermo fisher scientific	Cat# EC68852BOX
TBE-Urea Sample Buffer	Thermo fisher scientific	Cat# LC6876

**CONTACT FOR REAGENT AND RESOURCE SHARING**

Further contact information and requests for resources and reagents should be directed to and will be fulfilled by the Lead Contact, Leifu Chang ([lchang18@purdue.edu](mailto:lchang18@purdue.edu)).

**EXPERIMENTAL MODEL AND SUBJECT DETAILS**

The plasmid DNAs were amplified in *E. coli* DH5 $\alpha$  cells. Cas12a and AcrVA proteins were expressed in *E. coli* BL21-CodonPlus (DE3)-RIL cells cultured at 37°C or 18°C in TB medium.

**METHOD DETAILS****Protein Expression and Purification**

The plasmids harboring full-length LbCas12a or AcrVA4 is obtained from Addgene. LbCas12a or AcrVA4 is fused with an N-terminal 10xHis tag and the following maltose binding protein (MBP) tag (Chen et al., 2018; Watters et al., 2018). The genes encoding full-length AcrVA1 and AcrVA5 were cloned into the pET28-MKH8SUMO vector. The resultant plasmids were individually transformed into BL21-CodonPlus (DE3)-RIL cells for overexpression. A single colony was picked for overnight small-scale culture and then inoculated in 1-liter TB medium. The cells were induced by adding 0.3 mM isopropyl  $\beta$ -D-thiogalactopyranoside (IPTG) and grown at 18°C overnight. The cells were harvested and then resuspended in buffer A (25 mM Tris-HCl, pH 8.0, 2 M NaCl, 1 mM PMSF, 5 mM 2-mercaptoethanol and 10  $\mu$ L benzonase). After sonication and centrifugation, the supernatants were incubated with Ni-NTA resin for 1 hour. The resin was washed with buffer A containing 30 mM imidazole, and then the target protein was eluted with 10 mL elution

buffer (25 mM Tris-HCl, pH 7.0, 1 M NaCl, 5% Glycerol, 5 mM 2-mercaptoethanol, 300 mM imidazole). TEV was added to remove the His-MBP or His-SUMO tag. The target proteins were further purified by ion-exchange chromatography (HiTrap Q for AcrVA1, AcrVA4 and AcrVA5 and HiTrap SP for LbCas12a) and eluted with a linear sodium chloride gradient. Further purification steps were performed using gel filtration (Superdex 200) equilibrated with buffer B containing 25 mM Tris-HCl pH 8.0, 150 mM NaCl, 5 mM DTT. Peak fractions were concentrated and stored in -80°C.

### Mutagenesis

All mutations were generated by PCR-based QuikChange site-directed mutagenesis method. All mutants were confirmed by DNA sequencing. The mutant proteins were expressed and purified as described for WT.

### Size Exclusion Chromatography

The LbCas12a and AcrVA proteins were separately purified before the SEC assays. To reconstitute LbCas12a-AcrVA complexes, AcrVA proteins were mixed with LbCas12a at a ratio of 5:1 at 20°C for 30 mins. To reconstitute LbCas12a-crRNA-AcrVA complexes, the crRNA synthesized from IDT was incubated with LbCas12a at a ratio of 1.2:1 on ice for 30 mins. AcrVA proteins were then added to the ribonucleoprotein complex at a ratio of 5:1 for another 30 mins. The mixture was applied to a Superdex 200 (GE) column equilibrated with buffer B (25 mM Tris-HCl, pH 8.0, 150 mM NaCl and 5 mM DTT). SDS-PAGE was used to analyse and monitor the complex formation.

### In Vitro DNA Cleavage Assay

Target DNA containing the 5'-TTTA-3' PAM was synthesized and inserted into pET28-MHL vector. The resultant plasmids were then linearized by FspI (NEB) and purified by PCR purification columns (QIAGEN). For cleavage assays, the LbCas12a-crRNA ribonucleoproteins (50 µg) purified from gel-filtration was diluted into the cleavage buffer (25 mM Hepes, pH 7.0, 150 mM KCl, 5 mM MgCl<sub>2</sub>, 5 mM DTT, 5% glycerol). The linearized plasmids (200 ng) and AcrVA1 (50 pM, 125 pM, 0.25 nM, 0.5 nM and 1 nM) or AcrVA4 (125 pM, 0.25 nM, 0.5 nM, 1 nM and 2 nM) proteins were added into the cleavage buffer simultaneously. The mixture was incubated at 37°C for 30 mins. EDTA (40 mM) and Proteinase K (1 µl) were then added to stop the reaction. The cleavage products were resolved on 0.8% TBE agarose gels and visualized by ethidium bromide staining. The mutant protein assay was performed similarly to wide-type in the presence of 125 pM AcrVA1 or 0.25 nM AcrVA4 proteins.

### crRNA Cleavage Assay

LbCas12a (1.5 µg) was pre-incubated with crRNA at a ratio of 2:1 at 37°C in the cleavage buffer (25 mM Tris-HCl, pH 8.0, 150 mM KCl, 5 mM MgCl<sub>2</sub>, 5 mM DTT, 5% glycerol). AcrVA1 proteins (2.5 pM) were then added into the mixture for another 30 mins. The reaction was denatured with TBE-urea loading buffer at 85°C for 10 mins, and separated on a 15% TBE-urea gel and stained using SYBR Gold (Invitrogen).

### Isothermal Titration Calorimetry

The AcrVA4 and LbCas12a proteins were expressed and purified as described above. To obtain the LbCas12a-crRNA binary complex, LbCas12a proteins were incubated with crRNA at a 1:1.2 molar ratio and then loaded to the Superdex 200 column to remove excess crRNA. All ITC experiments were carried out in buffer containing 25 mM Tris, pH 8.0, 150 mM NaCl using MicroCal iTC200 system (Malvern, UK) at 25°C. The concentrations of AcrVA4 and LbCas12a-crRNA were 600 µM and 20 µM, respectively. The results were analyzed with Origin software.

### Electrophoretic Mobility Shift Assay

EMSA were performed in the reaction buffer containing 25 mM Tris pH 8.0, 150 mM NaCl, 5 mM MgCl<sub>2</sub>, 5 mM DTT and 5% glycerol. The inactive LbCas12a (D832A) plasmid was obtained from Addgene ([Chen et al., 2018](#)). The purified LbCas12a mutant proteins (1.0 µg) were incubated with crRNA at a ratio of 1:1.1 on ice for 30 mins and then mixed with AcrVA4 (60 pM) for 10 mins. The target DNA (80 ng) was added into the mixture for another 30 mins. The sample was loaded onto a 0.8% TAE agarose gel and run 1 hour at 60 V at 4°C. The gels were visualized by staining with ethidium bromide.

### Electron Microscopy

Aliquots of 3 µL LbCas12a complexes at ~3.0 mg/ml were applied to glow-discharged Quantifoil holey carbon girds (R2/2, 400 mesh). For LbCas12a-crRNA-AcrVA1 complex, an additional 5 times AcrVA1 was added and incubated for 30 mins on ice. The grids were blotted for 6 s and plunged into liquid ethane using a Gatan Cryoplunge 3 plunger. Cryo-EM data were collected with a Titan Krios microscope (FEI) operated at 300 kV and images were collected using Leginon ([Suloway et al., 2005](#)) with a nominal magnification of 130,000x (resulting in a calibrated physical pixel size of 1.06 Å/pixel) or 105,000 x (for LbCas12a-crRNA structure) and a defocus range of 1.5–3.2 µm. The images were recorded on a K2 summit electron direct detector in super-resolution mode at the end of a GIF-Quantum energy filter operated with a slit width of 20 eV. A dose rate of 5 e-/pix/s and an exposure time of 8 seconds were used, generating 40 movie frames with a total dose of ~35 electrons per Å<sup>2</sup>. A total of 877, 1,760, 3,000, 1,514, and 1866 movies stacks were collected for LbCas12a-crRNA, LbCas12a-crRNA-AcrVA1, LbCas12a-crRNA-AcrVA4-AcrVA5, LbCas12a-crRNA-AcrVA4 and Cas12a-crRNA-AcrVA4-DNA complexes, respectively ([Tables S1 and S2](#)).

### Image Processing

Movie frames were aligned using MotionCor2 (Zheng et al., 2017) integrated into the Appion data-processing pipeline (Lander et al., 2009) before subsequent processing. A binning factor of 2 was used in this step. The summed individual micrographs were imported to RELION-3 (Zivanov et al., 2018) and contrast transfer function (CTF) parameters were estimated using Gctf (Zhang, 2016). Initially, about 5000 particles were manually picked to generate 2D averages, which were used as template for subsequent auto-picking.

For LbCas12a-crRNA-AcrVA1 complex, about 1.36 million particles were auto-picked and extracted from the dose weighted micrographs. The dataset was split into parts of 60,000 particles for 2D classifications, which were used to exclude false and bad particles that fall into 2D averages with poor features. After this cleaning step, 755,000 particles remained. The dataset was split into two parts for 3D classification. Each part was classified into 6 classes, resulting in one best class with good quality and density for AcrVA1. 157,000 particles from good classes were combined to perform 3D refinement, converging at 3.8 Å resolution. 3D refinement after Bayesian polishing produced a map at 3.63 Å resolution. CisTEM auto-refinement on the same polished particles converged at a 3.49 Å resolution. Further 3D classification of the polished particles revealed a class with 19% particles that showed an additional density assigned to a second AcrVA1. This class was refined to a resolution of 4.3 Å.

For LbCas12a-crRNA-AcrVA4-AcrVA5 complex data, a similar data processing strategy was used. After 2D classification, 1.5 million particles were selected from 1.8 million auto-picked particles. After 3D classification, remaining 800,000 particles were used for 3D refinement and Bayesian polishing. Polished particles were combined and classified in 6 classes by 3D classification. From the classification, maps containing one or two copies of LbCas12a-crRNA molecules can be discerned and named as LbCas12a-crRNA-(AcrVA4)<sub>2</sub> and (LbCas12a-crRNA-AcrVA4)<sub>2</sub>, respectively. For the LbCas12a-crRNA-(AcrVA4)<sub>2</sub> class, further processing including 3D refinement, CTF refinement, Bayesian polishing and 3D refinement were performed, resulting in a map at 3.44 Å resolution. CisTEM auto-refinement (Grant et al., 2018) on the same particles converged at 3.38 Å resolution. For the (LbCas12a-crRNA-AcrVA4)<sub>2</sub> class, particles were re-centered to the center of mass using an in-house script based on 2D averages. Further processing including 3D refinement with C2 symmetry, CTF refinement, Bayesian polishing and 3D refinement with C2 symmetry was performed, resulting in a map at 3.67 Å resolution. CisTEM auto-refinement with C2 symmetry converged at 3.38 Å resolution.

For LbCas12a-crRNA, LbCas12a-crRNA-AcrVA4 and Cas12a-crRNA-AcrVA4-DNA datasets, similar procedures were performed. Cryo-EM image processing is summarized in Table S1.

### Model Building and Refinement

Structures of AcrVA1 and AcrVA4 were build *de novo* in COOT (Emsley et al., 2010). For Cas12a-crRNA, crystal structure (PDB: 5ID6) was initially fitted into cryo-EM maps and rebuilt manually in COOT (Emsley et al., 2010). Model refinement was performed using phenix.real\_space\_refine tool in Phenix (Afonine et al., 2018). The refinement statistics are summarized in Table S2.

### Visualization

Figures were generated using PyMOL and Chimera (Pettersen et al., 2004). Movies are prepared in PyMol. Structural conservation figures were generated using ConSurf (Ashkenazy et al., 2010).

### DATA AND SOFTWARE AVAILABILITY

Cryo-EM reconstruction of Cas12a-crRNA, Cas12a-crRNA-AcrVA1, Cas12a-crRNA-(AcrVA1)<sub>2</sub>, Cas12a-crRNA-(AcrVA4)<sub>2</sub>, (Cas12a-crRNA-AcrVA4)<sub>2</sub>, Cas12a-crRNA-(AcrVA4)<sub>2</sub>-DNA and (Cas12a-crRNA-AcrVA4-DNA)<sub>2</sub> have been deposited in the Electron Microscopy Data Bank under the accession numbers EMD-0449, EMD-0447, EMD-0446, EMD-0445, EMD-9398, EMD-20132 and EMD-20182 respectively. Coordinates for atomic models of Cas12a-crRNA, Cas12a-crRNA-AcrVA1, Cas12a-crRNA-(AcrVA1)<sub>2</sub>, Cas12a-crRNA-(AcrVA4)<sub>2</sub>, (Cas12a-crRNA-AcrVA4)<sub>2</sub>, Cas12a-crRNA-(AcrVA4)<sub>2</sub>-DNA complex have been deposited in the Protein Data Bank under the accession numbers 6NME, 6NMD, 6NMC, 6NMA, 6NM9 and 6OMV respectively.